Electronic Supplementary Information

Mechanism for the Enhanced Oxygen Reduction Reaction of $La_{0.6}Sr_{0.4}Co_{0.2}Fe_{0.8}O_{3-\delta}$ by Strontium Carbonate

Mei Li,[a,1] Zhongti Sun,[a,1] Wenqiang Yang,[a] Tao Hong,[a] Zhesheng Zhu,[a] Yanxiang Zhang,[b] Xiaojun Wu,[a,c,] Changrong Xia[a, *]*

[a]*Key Laboratory of Materials for Energy Conversion, Chinese Academy of Sciences, Department of Materials Science and Engineering & Collaborative Innovation Center of Suzhou Nano Science and Technology, University of Science and Technology of China, No. 96 Jinzhai Road, Hefei, Anhui Province, 230026, P. R. China*

[b]*School of Materials Science and Engineering, Harbin Institute of Technology, Harbin, Heilongjiang 150001, China.*

[c]*Hefei National Laboratory of Physical Sciences at the Microscale, Synergetic Innovation of Quantum Information & Quantum Technology, University of Science and Technology of China, No. 96 Jinzhai Road, Hefei, Anhui Province, 230026, P. R. China*

[1]*: The first author.*

* Corresponding: xiacr@ustc.edu.cn; xjwu@ustc.edu.cn

Experimental Details

Powder preparation LSCF powder was synthesized using a combustion process with $La(NO_3)_3$(99.9%), $Sr(NO_3)_2$ (99.5%), $Co(NO_3)_3{\cdot}6H_2O$ (99.0%) and $Fe(NO_3)_3{\cdot}9H_2O$ (98.5%) as the cation precursors whereas ethylenediaminetetraacetic acid (EDTA, 99.5%) and citric acid (99.5%) as the combustion agents. Stoichiometric amounts of the cation precursors to the nominal composition were dissolved in distilled water. The combustion agents were subsequently added to the nitrate solution with a molar ratio of 1:1:2 for the total metal ions, EDTA, and citric acid, respectively. Whereafter, ammonia was added to adjust pH to about 6.0. The precursor solution was subsequently heated on a hot plate till self-combustion occurred. After the rapid and self-sustaining combustion, the resulting black ash was collected and then heated at 900 °C for 2 h. Finally, the desired LSCF phase was obtained with a well-defined crystalline perovskite structure.

SDC powder was prepared with the carbonate co-precipitation method[1] using $Sm(NO_3)_3$ (99.95%) and $Ce(NO_3)_3$ (99%) as the cation sources, and ammonia carbonate (99.7%) as the precipitant. The precipitates were dried at 90 °C and then heated at 600 °C for 2 h to obtain SDC powders with fluorite structure. All chemicals were from Sinopharm Chemical Reagent Co. Ltd.

Single cell fabrication and test Anode supported single cells consisting of Ni-$Zr_{0.85}Y_{0.15}O_{1.925}$ (YSZ) anodes, YSZ electrolytes, SDC inter-layers, and LSCF based cathodes were fabricated to further characterize the $SrCO_3$ effect on ORR. YSZ powder was prepared by glycine-nitrate method[2] using $Y(NO_3)_3{\cdot}6H_2O$ (99.99%) and $Zr(NO_3)_4{\cdot}5H_2O$ (99%) as the precursors, then glycine (99.5%) was subsequently added to the nitrate solution. The molar ratio of metal ion to glycine was 2:1. The solution was stirred for 2 h with magnetic stirring apparatus, and then heated on a hot plate until self-combustion occurred. NiO powder was also synthesized by glycine-nitrate method with $Ni(NO_3)_2{\cdot}6H_2O$ (98.0%) in the same process. The as-prepared ashes of YSZ and NiO were then heated at 750 °C and 850 °C for 4 hours, respectively, to obtain the required powders. The details of fabrication process for half cells with the SDC interlayer depositing on the YSZ electrolyte have been previously reported.[3]. Finally, cathode slurry was screen printed on the surface of SDC layer and co-heated at 1000 °C for 2 h. The four-layered pellets were then sealed onto the top of a ceramic tube with the cathode side exposing to ambient air, and the anode side to flowing humidified (~ 3% H_2O) hydrogen at 50 mL·min^{-1}, respectively.

Thermogravimetry Analysis

Figure S1 shows the TG curve of $Sr(AC)_2$, which is measured in air from room temperature to 1400 °C. The first weight loss of 4.14% starts at 160 °C and finishes at 280 °C, which should be caused by the loss of physical and chemical absorbed water. A weight loss of 26.8% begins at about 370 °C, corresponding $Sr(Ac)_2$ decomposition to $SrCO_3$, and ends at 525 °C, at which $Sr(Ac)_2$ is completely changed to $SrCO_3$. At the temperature in the range from 550 to 800 °C, $SrCO_3$ is thermally stable in air. At 815 °C, it starts to decompose into SrO with a loss of 20.47%.

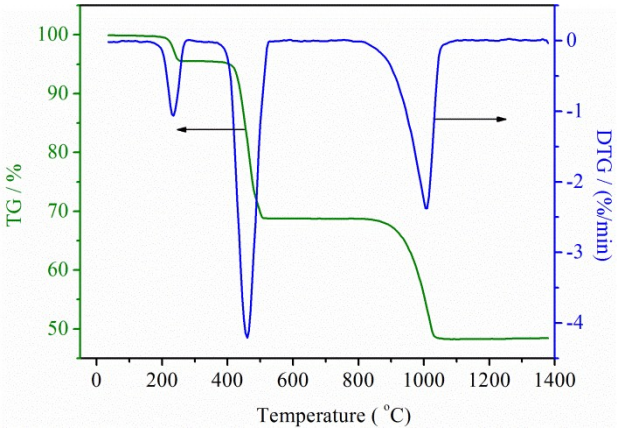

Figure S1. TG and DTG curves for $Sr(AC)_2$ measured in air from room temperature to 1400 °C.

XRD of the powders

For the measurement of XRD for the single phases, Figure S2(a, c, e), LSCF powder is heated at 900 °C for 2 h, and $Sr(Ac)_2$ powder is heated at 750 °C for 5h, meanwhile, SDC powder is heated at 600 °C for 2 h. For the measurement of XRD for the composite phases, Figure S2(b, d), the LSCF-$SrCO_3$ and SDC-$SrCO_3$ composites are formed by grinding the two phases with the weight ratio of 1:1, and all the composites are co-heated at 750 °C for 5 h.

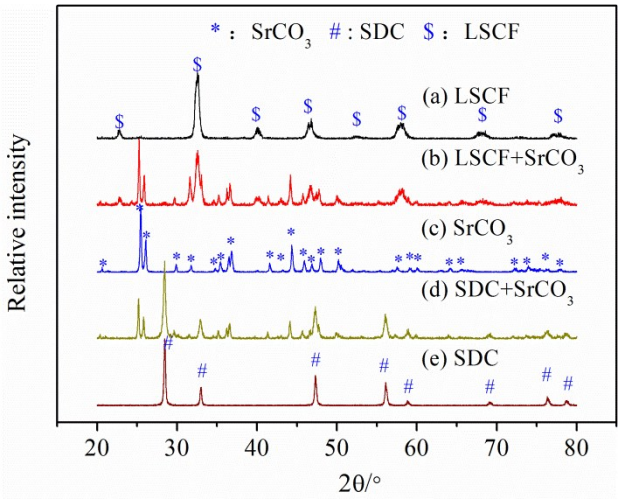

Figure S2. XRD patterns of (a) LSCF powder, (b) LSCF-$SrCO_3$ composite, (c) $Sr(Ac)_2$ powder, (d) SDC-$SrCO_3$ composite, and (e) SDC powder.

Structure of LSCF cathode

Figure S3a shows the fractured cross-sectional microstructures of a bare LSCF electrode, which is used for the measurement of electrochemical impedance spectroscopy. The porous LSCF consists of grains with size from 0.1 to 0.3 um. When 8.0 wt. % $SrCO_3$ is infiltrated, the nanoparticles, about 60 nm in size, are seen to distribute homogeneously on the inner surface of the porous LSCF, Figure S3b.

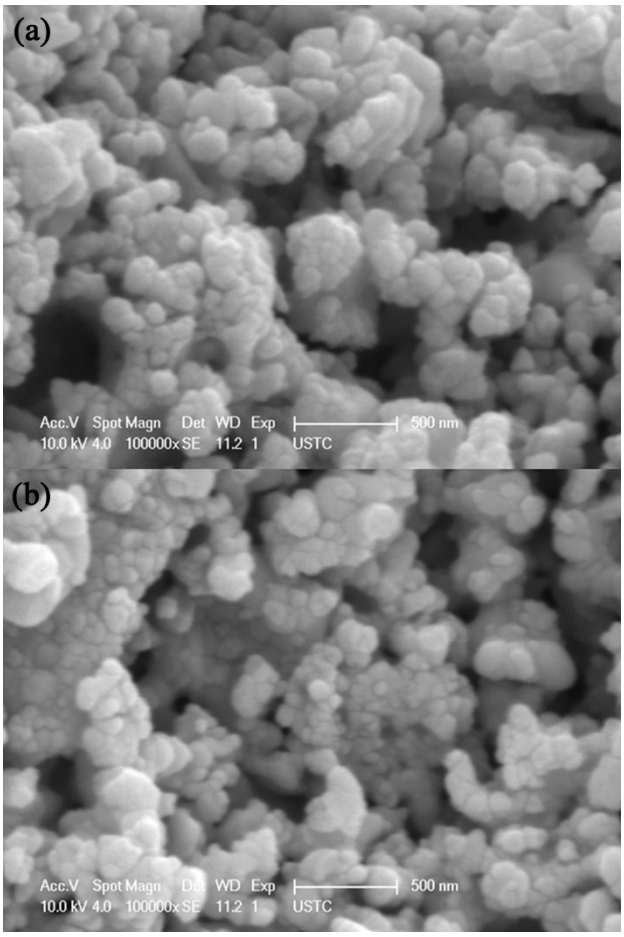

Figure S3. SEM micrographs for (a) a bare LSCF cathode and (b) LSCF electrode infiltrated with 8.0 wt. % $SrCO_3$.

Cathode Reaction Process

To explore the oxygen reduction processes, four different oxygen partial pressures ($P_{O_2} = 0.05, 0.1, 0.21, and\ 1$ atm) are applied for the electrochemistry impedance spectrum measurement on symmetrical cells in open circuit conditions at 700 °C. Figure S4a shows the electrical impedance spectra (EIS). To reveal the effect of oxygen partial pressure on the impedance spectra, the distribution of relaxation time (DRT) method[4-7] is used. Figure S4b shows the *F(τ)* distribution of the logarithm for relaxation times *τ*. The area under each peak is the polarization resistance corresponding to the sub-process, and the DRT curves are fitted well with three peaks, i.e. peak 1, peak 2 and peak 3. The fitting results of the area under the each peak (R_1, R_2, and R_3, respectively) are plotted in Figure S4c as a function of P_{O_2}.

To deep into characterizing the sub-processes for bare LSCF, the equation of $R_i = kP_{O_2}^{-n}$ is used to illustrate the relationships between the resistance R_i and oxygen partial pressure P_{O_2}, where *k* is a constant, and *n* is the parameter determining the rate-determining step.[8, 9] The EIS data measured at different P_{O_2} are fitted well as suggested by the DRT results. The value of *n* for R_1 (n1) attributed to the resistance for the high-frequency response is 0.1, closed to 0.125, which corresponds to the charge transfer process (Eq. 1).[10] Meanwhile, the value of *n* for R_2 (n2) ascribed to the resistance for medium-frequency response is 0.28, closed to 0.25, suggesting that this sub-step is dominated by oxygen incorporate process (Eq. 2).[8, 9] In addition, the impedance of the low frequency response (R_3) has a dependence (n3) on oxygen partial pressure of 0.89, which is close to 1.0, therefore, the sub-step for the electrode reaction can be described as the oxygen gas diffusion within the electrode (Eq. 6).[11]

$$O^- + e^- + V_O^{\bullet\bullet} \leftrightarrow O_O^x \quad (1)$$

$$O_{2,ad} + 2e^- + V_O^{\bullet\bullet} \leftrightarrow 2O_O^x \quad (2)$$

$$O_2(g, bulk) \leftrightarrow O_2(g, interface) \quad (3)$$

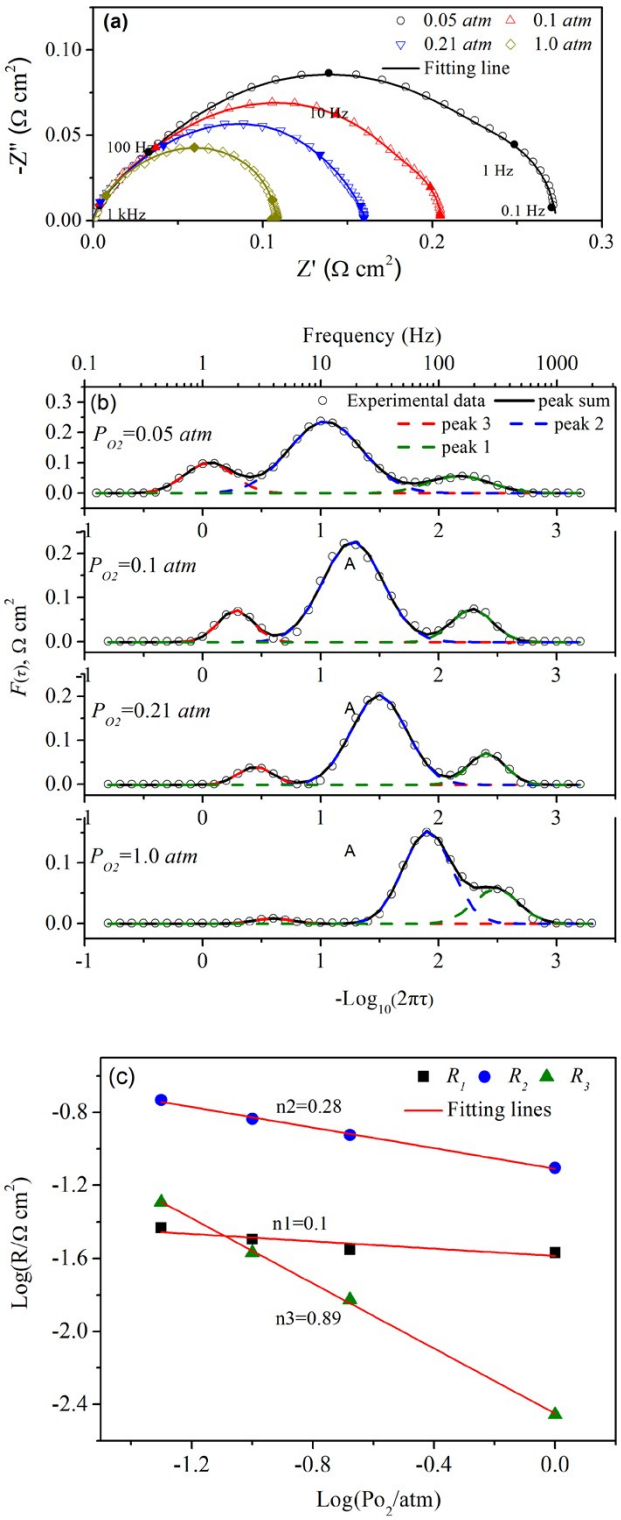

Figure S4 (a) Electrochemical impedance spectra measured at 700 °C under different oxygen partial pressures (P_{O_2}) for the symmetrical cells with LSCF electrodes, (b) DRT analysis of the EIS data in Figure S4a, and (c) Fitted R versus oxygen partial pressure.

Single Cell Performance Enhanced with $SrCO_3$

To further evaluating the enhancement for ORR, electrochemical performance is compared for a bare LSCF cathode and an electrode infiltrated with 5.6 wt. % $SrCO_3$ using single cell configuration with humidified H_2 (~ 3% H_2O) as the fuel and ambient air as the oxidant.

Figure S5 shows the cell voltage and power density as a function of current density. The single cell with the bare LSCF cathode generates a peak power density of 1.08 Wcm^{-2} at 750 °C, Figure S5a, which is almost equal to the result reported by Liu *et al.*[12] The peak power density increases to 1.25 Wcm^{-2} when the cathode is infiltrated with 5.6 wt. % $SrCO_3$, Figure S5b. The performance of the cell with the LSCF-$SrCO_3$ cathode is comparable with those using composite cathode such as GDC-LSCF and LCC-LSCF.[12, 13] The single cell with $SrCO_3$ shows much lower interfacial polarization resistance than the bare LSCF, Figure S5c. For example, the resistance is reduced from 1.74 to 1.14 Ω cm^2 at 600 °C. Since the two cells have the same anode and electrolyte, the reduction in polarization resistance and increase in power density must be caused by the cathode, i.e. $SrCO_3$ nanoparticles. Figure S5d shows the primary durability test, which demonstrates that the LSCF-$SrCO_3$ electrodes are relatively stable in the 150 h measuring at a constant current density of 200 $mAcm^{-2}$ at 700 °C.

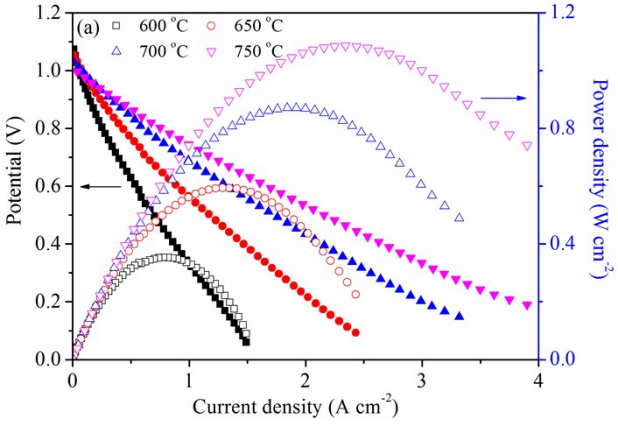

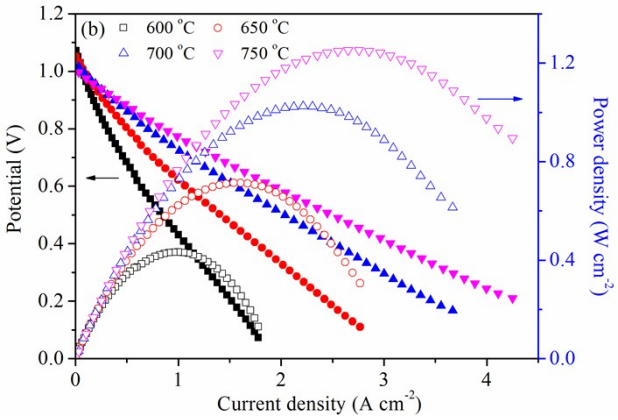

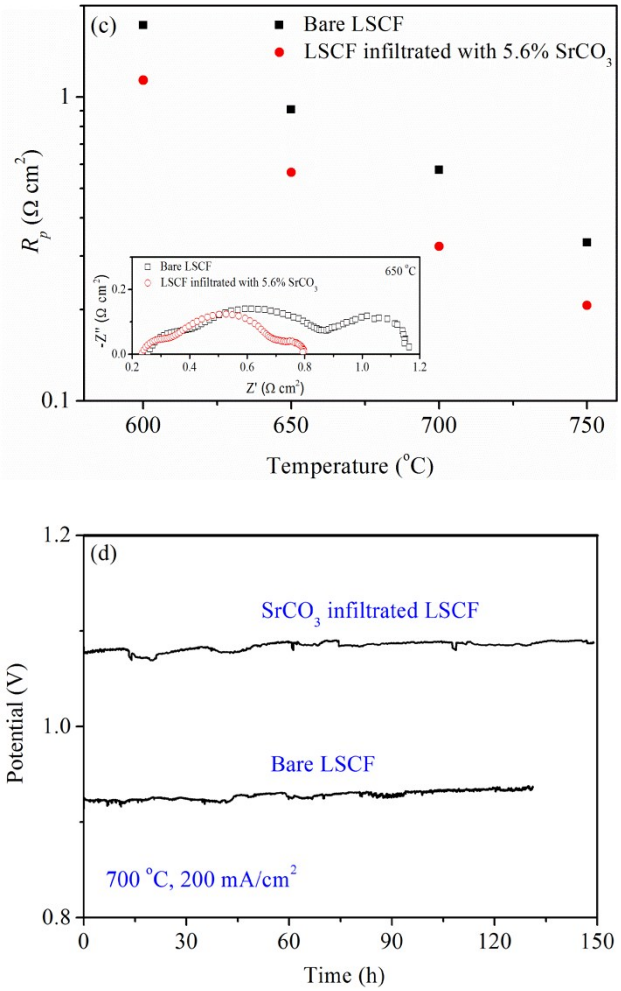

Figure S5. Performance of anode-supported single cells measured at 600-750 °C using humidified hydrogen (~3% H_2O) as the fuel and ambient air as the oxidant. (a) The cell voltage and power density as a function of current density for a cell with the bare LSCF cathode, (b) with the LSCF cathode infiltrated with 5.6 wt. % $SrCO_3$, (c) total interfacial polarization resistance which determined from EIS as shown with the insert, and (d) durability test at a constant current density of 200 $mAcm^{-2}$ at 700 °C.

Computational Details

All the calculations were performed by a spin-polarized density functional theory (DFT) based on a plane wave basis set, implemented by Vienna ab-initio simulation package (VASP).[14, 15] The electron-ion interactions were indicated by the projector augmented wave (PAW) method,[16] the exchange and correlation effects were treated by the generalized gradient approximation with the Perdew-Burke-Ernzerhof (PBE) functional.[17] The kinetic cutoff energy was 400 eV, the total energy convergence was set to less than 10^{-4} eV, and the force convergence criterion was smaller than -0.03eV/Å. Electron smearing of σ=0.05 eV was used following the Methfessel-Paxton scheme,[18] Brillouin zone sampling was employed by a Monkhorst-Packing grid.[19] 2×2×1 k-points was used for the slab optimizations. Dipole correction was also used for the LSCF (100) and $SrCO_3$ cluster adsorption on LSCF (100) surface.[20] The Bader charge analysis was used to get the increased and reduced charge on the LSCF (100) surface.[21] Climb Image Nudged Elastic Band (CI-NEB)[22] method is used to obtain the energy barrier of O_2 dissociation.

A model of $La_{0.625}Sr_{0.375}Co_{0.25}Fe_{0.75}O_{3-\delta}$ was used to describe the experimental model ($La_{0.6}Sr_{0.4}Co_{0.2}Fe_{0.8}O_{3-\delta}$) in this work, which has been used in our previous simulation, as shown in Figure S6.[23] As LSCF (100) surface is the most stable one, we use six-layer (100) slab exposed to Co and Fe atoms, the bottom three atom layers are fixed, while the rest are fully relaxed. Meanwhile, the vacuum layer thickness is about 15 Å.

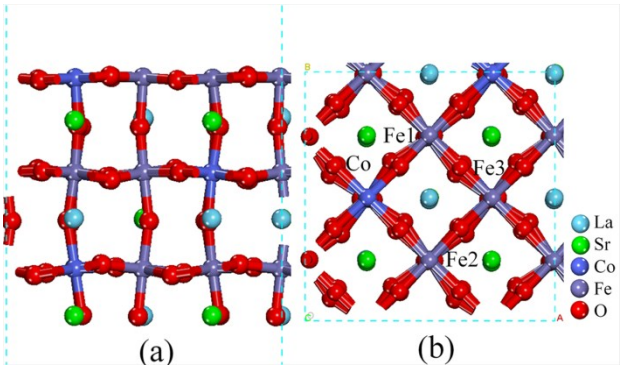

Figure S6. Side (a) and top (b) views of LSCF (100) surface.

Based on the experiments, the $SrCO_3$ cluster would adsorb on the LSCF surface. Considering the limit of computational resources, a $SrCO_3$ cluster composing of four $SrCO_3$ formula units is used, as shown in Figure S7.

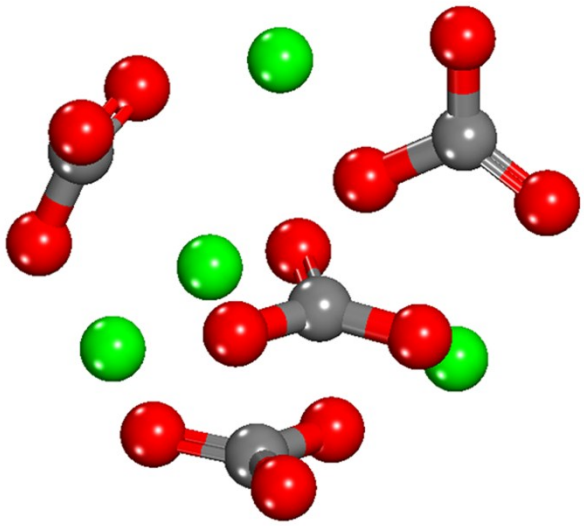

Figure S7. $SrCO_3$ cluster structure composing of four $SrCO_3$ formula units. Carbon, oxygen, and strontium atom are marked in grey, red, and green.

As shown in Figure. S6, two adsorption sites on the LSCF (100) surface are taken into account, where one is the site involving Fe1, Fe2 and Fe3 atom, named as Fe-Fe site, and the other is the site involving Fe1, Fe2, and Co atom, named as Co-Fe site. The adsorption configurations and total energy are illustrated in Figure S8 and Table S1, respectively. It is clear, $SrCO_3$ cluster prefer to adsorb on Co-Fe site, which is more stable than that on Fe-Fe site with energy difference of 0.54 eV.

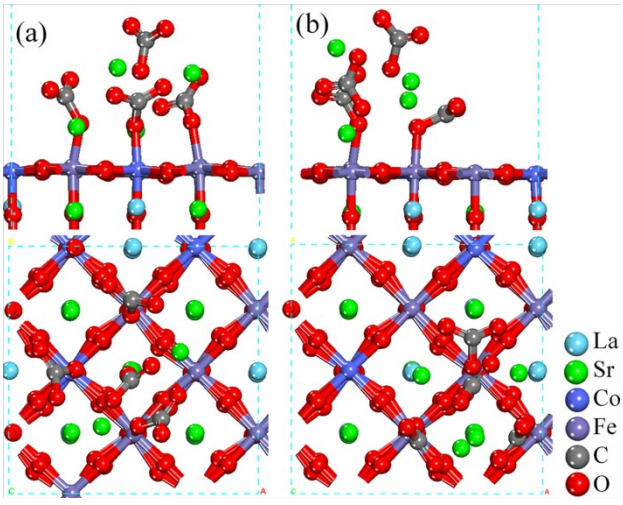

Figure S8. The side and top view of the $SrCO_3$ cluster adsorbed on the LSCF (100) surface on (a) Fe-Fe and (b) Co-Fe site.

Table S1. Total energy and energy change of adsorption configuration with $SrCO_3$ cluster on the LSCF (100) surface

Conf.	*E*/eV	*ΔE*/eV
Fe-Fe	-1026.36	0
Co-Fe	-1026.90	-0.54

On $SrCO_3$-modified LCSF (100) surface, three Fe-sites closed to the interface, *i.e.,* Fe-3, Fe-4, and Fe-5, are considered for the adsorption of O_2. The corresponding adsorption energies and structures are shown in Table S2 and Figure S9, respectively. The adsorption energy is defined as $E_{ads}=E_{total}-E_{slab}-E_{O2}$, in which E_{total} and E_{slab} are the total energy of the $SrCO_3$-LSCF with and without O_2 adsorption, E_{O2} is the energy of free O_2 molecule. The most stable site is Fe-5 site with the adsorption energy of -0.74 eV. Then, the dissociation adsorption of O_2 on two neighboring Fe sites (Fe-Fe site) or neighboring Fe and Co sites (Fe-Co site) are considered, as shown in Figures S10. It is clear that he dissociated adsorption of O_2 on Fe-Fe site (-1.61 eV) is more energetically favorable than that on Fe-Co site (-1.25 eV), as summarized in Table S3.

Table S2. Adsorption energy of O_2 on $SrCO_3$-LSCF about Fe-3, Fe-4, and Fe-5 configurations.

Conf.	E_{ads}/eV	*ΔE*/eV
Fe-5	-0.74	0.00
Fe-4	-0.34	0.40
Fe-3	-0.29	0.45

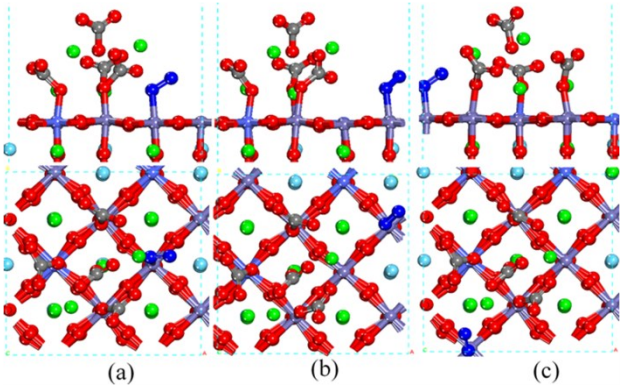

Figure S9. Adsorbed configuration of O_2 on the $SrCO_3$-impregnated LSCF, from left to right (a, b, c), Fe-3, Fe-4,

and Fe-5 configurations. Adsorbed oxygen atoms in blue, other atoms are referred the $SrCO_3$-LSCF model.

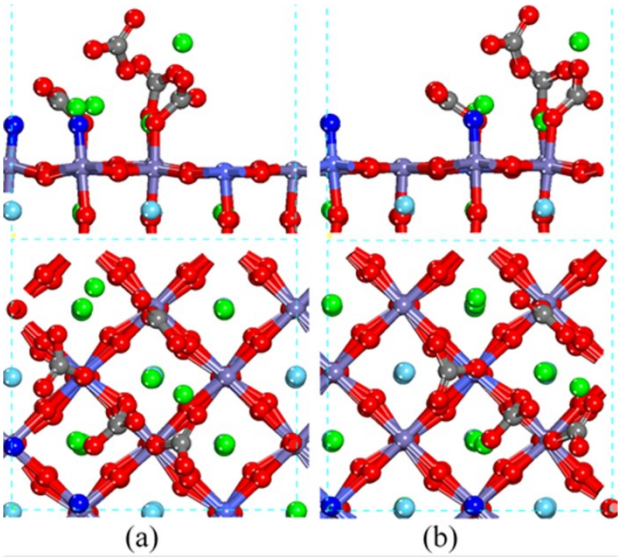

Figure S10. Dissociated configuration of O_2 on the Fe-5 model. From left to right (a, b), Fe-Fe and Fe-Co dissociated configurations. Such as Fe-Fe model means that the two dissociated oxygen atoms on the two close Fe atoms. Adsorbed oxygen atoms in blue, other atoms are referred the $SrCO_3$-LSCF model.

Table S3. Dissociated energy of O_2 on the Fe-5 model

Conf.	E_{ads}/eV	ΔE/eV
Fe-Fe	-1.61	0.00
Fe-Co	-1.26	0.35

X-ray Photoelectron Spectroscopy(XPS) Analysis

XPS analyses of bare LSCF powder and modified LSCF powder are performed on a photoelectron spectrometer (ESCALAB 250Xi) at room temperature. Where the modified LSCF powder is the LSCF powder infiltrated with 2 wt.% $SrCO_3$. Figure S11 show the O 1s spectra and the deconvolution results. The O 1s spectra for all the samples present two peaks with the binding energy values at 528.6 and 531.3 eV. The O 1s signal can be decomposed into four peaks, centered at 528.6, 530.6, 531.5 and 533.1 eV. The lower binding energy (528.6 eV) peak should be ascribed to the lattice oxygen species, O^{2-}, and the higher binding energy (533.1 eV) peak is assigned to molecular water adsorbed on the surface. In addition, peak at 530.6 eV is assigned to adsorbed oxygen species, O^-, whereas peak at 531.5 eV comes from hydroxyls species, OH^- and from carbonate species, CO_3^{2-}.[24]

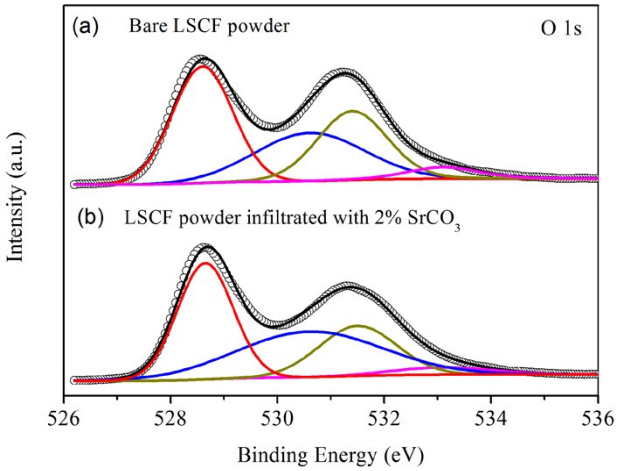

Figure S11. XPS results of O 1s peak of bare LSCF powder (a), and LSCF powder infiltrated with 2 wt.% $SrCO_3$ (b). The relative content (molar fraction) of the different kinds of oxygen species over the total surface oxygen amount can be estimated from the relative area of these sub-peaks, Table S4. The relative content of O^- increase with the addition of $SrCO_3$, the result is consistent with the analysis of DFT. Meanwhile, as the electrophilic reactant, O^- is very important in the ORR process. In addition, as the surrounding environment is stationary, we set adsorbed water as the reference, the ratios between surface oxygen species and adsorbed water further confirm the increase of O^- with the infiltration of $SrCO_3$. And the almost unchanged value of (OH^-, CO_3^{2-})/H_2O illustrates the absorbability of OH^- and CO_3^{2-} is constant.

Table S4. O 1s-XPS peak deconvolution results in percentage and the surface concentration ratio of adsorbed water

	O^{2-} (Lattice)	O^-	OH^-, CO_3^{2-}	H_2O	O^{2-}/H_2O	O^-/H_2O	(OH^-, CO_3^{2-})/H_2O
Bare LSCF	38.7	28.7	27.6	5.0	7.74	5.74	5.52
Infiltrated LSCF	36.6	37.4	22.0	4.0	9.15	9.35	5.50

Reference

1. D. Ding, B. Liu, Z. Zhu, S. Zhou and C. Xia, *Solid State Ionics*, 2008, **179**, 896-899.
2. Y. Wang, H. Zhang, F. Chen and C. Xia, *J. Power Sources*, 2012, **203**, 34-41.
3. L. Wu, S. Wang, S. Wang and C. Xia, *J. Power Sources*, 2013, **240**, 241-244.
4. J. Hayd and E. I.-T. ee, *J. Electrochem. Soc.*, 2013, **160**, F1197-F1206.
5. Y. Zhang, Y. Chen and F. Chen, *J. Power Sources*, 2015, **277**, 277-285.
6. Y. Zhang, Y. Chen, M. Yan and F. Chen, *J. Power Sources*, 2015, **283**, 464-477.
7. H. Sumi, T. Yamaguchi, K. Hamamoto, T. Suzuki and Y. Fujishiro, *J. Power Sources*, 2013, **226**, 354-358.
8. Y. Takeda, R. Kanno, M. Noda, Y. Tomida and O. Yamamoto, *J. Electrochem. Soc.*, 1987, **134**, 2656-2661.
9. M. J. Escudero, A. Aguadero, J. A. Alonso and L. Daza, *J. Electroanal. Chem.*, 2007, **611**, 107-116.
10. B. Kenney and K. Karan, *J. Electrochem. Soc.*, 2006, **153**, A1172-A1180.
11. X. J. Chen, K. A. Khor and S. H. Chan, *J. Power Sources*, 2003, **123**, 17-25.
12. M. Liu, D. Ding, K. Blinn, X. Li, L. Nie and M. Liu, *Int. J. Hydrogen Energy*, 2012, **37**, 8613-8620.
13. Y. Leng, S. Chan and Q. Liu, *Int. J. Hydrogen Energy*, 2008, **33**, 3808-3817.
14. G. Kresse and J. Furthmiiller, *Comp. Mater. Sci.*, 1996, **6** 15-50.
15. J. F. l. P. Ka¨ckell, and F. Bechstedt, *Phys. Rev. B*, 1996, **54**, 304-307.
16. J. J. Mortensen, L. B. Hansen and K. W. Jacobsen, *Phys. Rev. B,* 2005, **71**, 1-11.
17. John P. Perdew, Kieron Burke and M. Ernzerhof, *Phys. Rev. Lett.*, 1996, **77**, 3865-3868.
18. M. Methfessel and A. Paxton, *Phys. Rev. B*, 1989, **40**, 3616-3621.
19. H. J. M. a. J. D. Pack, *Phys. Rev. B,* 1976, **13**, 5188-5192.
20. L. Bengtsson, *Phys. Rev. B,* 1999, **59**, 12301-12304.
21. M. Yu and D. R. Trinkle, *J. chem. phys.*, 2011, **134**, 064111.
22. G. Henkelman, *J. Chem. Phys.,* 2000, **113** 9901-9904.
23. W. Yang, Z. Wang, Z. Wang, Z. Yang, C. Xia, R. Peng, X. Wu and Y. Lu, *ACS Appl. Mater. Interfaces*, 2014, **6**, 21051-21059.
24. N. A. Merino, B. P. Barbero, P. Eloy and L. E. Cadús, *Appl. Surf. Sci.*, 2006, **253**, 1489-1493.